Supplementary Material for

Assessing extreme total water levels across Europe for large-scale coastal flood analysis

Camila Cotrim[1], Alexandra Toimil[1], Iñigo J. Losada[1], Melisa Menéndez[1], Hector Lobeto[1]

[1]IHCantabria - Instituto de Hidráulica Ambiental de la Universidad de Cantabria, Santander, 30911, Spain

Sea level and wave datasets

This section describes the development and validation of the astronomical tide, storm surge and wave datasets used in this study.

Astronomical tide

TPXO is a global ocean tide model developed by Oregon State University. It provides a best fit to the Laplace Tidal Equations and along-track averaged data from TOPEX/Poseidon and Jason satellite missions. TPXO is a barotropic model of sea surface elevation and currents that employs a variational assimilation scheme, primarily using satellite altimetry data. The methods used to compute the model are described by Egbert et al. (1994) and further detail is provided by Egbert & Erofeeva (2002).
In this study, we used tidal constituents from the TPXO9 version 5 global tidal model (TPXO9v5). The TPXO9v5 database includes eight primary tidal constituents (M2, S2, N2, K2, K1, O1, P1, Q1), two long-period constituents (Mf, Mm), and three non-linear harmonic constituents (M4, MS4, MN4). These are provided at a spatial resolution of 1/30° (~3.5 km) near the coast and 1/6° (~16 km) offshore. The physical characteristics of these tidal constituents are then used to reconstruct hourly time series of tide level. The resulting astronomical tide time series are then validated against the tide component from 48 tide gauge records covering all European coasts. The sea level records from the tide gauges were obtained from the GESLA3 (Global Extreme Sea Level Analysis, version 3.0) database (Haigh et al., 2022). A harmonic analysis using the UTide tool (Codiga, 2011) was conducted to isolate the astronomical tide component and the non-tidal residual (NTR) component from the still water level (SWL) record measured by the tide gauges. Comparison of the tide simulated from the TPX09v5 outputs and measured by the tide gauges shows a near-perfect agreement, indicating a good non-stationary reconstruction of both, tidal amplitudes and phases.

Storm surge

Storm surge modeling was carried out using the Regional Ocean Modelling System (ROMS), developed by Rutgers University (Shchepetkin & McWilliams, 2005). The model was implemented over a European domain using an orthogonal grid, with a horizontal resolution ranging from 5 to 11 km. The computational domain extended from 30.943°W to 42.943°E in longitude, and from 25.05°N to 72.983°N in latitude, comprising a total of 272,382 grid nodes. The model configuration followed that of Cid et al. (2014). The Chapman scheme (Chapman, 1985) was applied to prescribe the free-surface boundary condition, and the Flather radiation condition (Flather, 1976) was used for the depth-integrated momentum components. Bottom friction was represented using a quadratic drag coefficient of 10^{-4}, and horizontal mixing was parameterized with a constant harmonic viscosity of 500 m^2/s. Hourly fields of surface wind and mean sea level pressure from the ERA5 reanalysis (Hersbach et al., 2020) were used as atmospheric forcing. Sea level boundary conditions were provided by tidal elevations and depth-averaged currents from TPXO9 tidal model, along with the inverse barometer effect from ERA5 mean sea level pressure fields.
To capture the non-linear interactions between tides and storm surges, a three-step simulation procedure was applied. First, a simulation of the SWLs was performed, in which both tidal and meteorological forcings were included to represent the full coupled dynamics. Second, a tide-only simulation was carried out using tidal constituents as boundary conditions, allowing

the astronomical tide to be isolated. Finally, storm surge levels were obtained by subtracting the astronomical tide from the SWL simulation.

Surge elevations were validated against 48 tide-gauge records along the European coasts. The validation between instrumental and numerical data was conducted using comparisons of time series, quantile–quantile plots, scatter plots, and several error metrics (e.g., bias, root mean square error - RMSE). Figure S1 shows an example for three tide-gauge stations of the storm surge hindcast and tide-gauge hourly time series over a six-month time window. Figure S2 shows scatter plots and quantile-quantile plots comparing the modeled surge elevations with the observed NTR from the tide gauges. The 75th, 90th, 95th, and 99.5th quantiles are indicated.

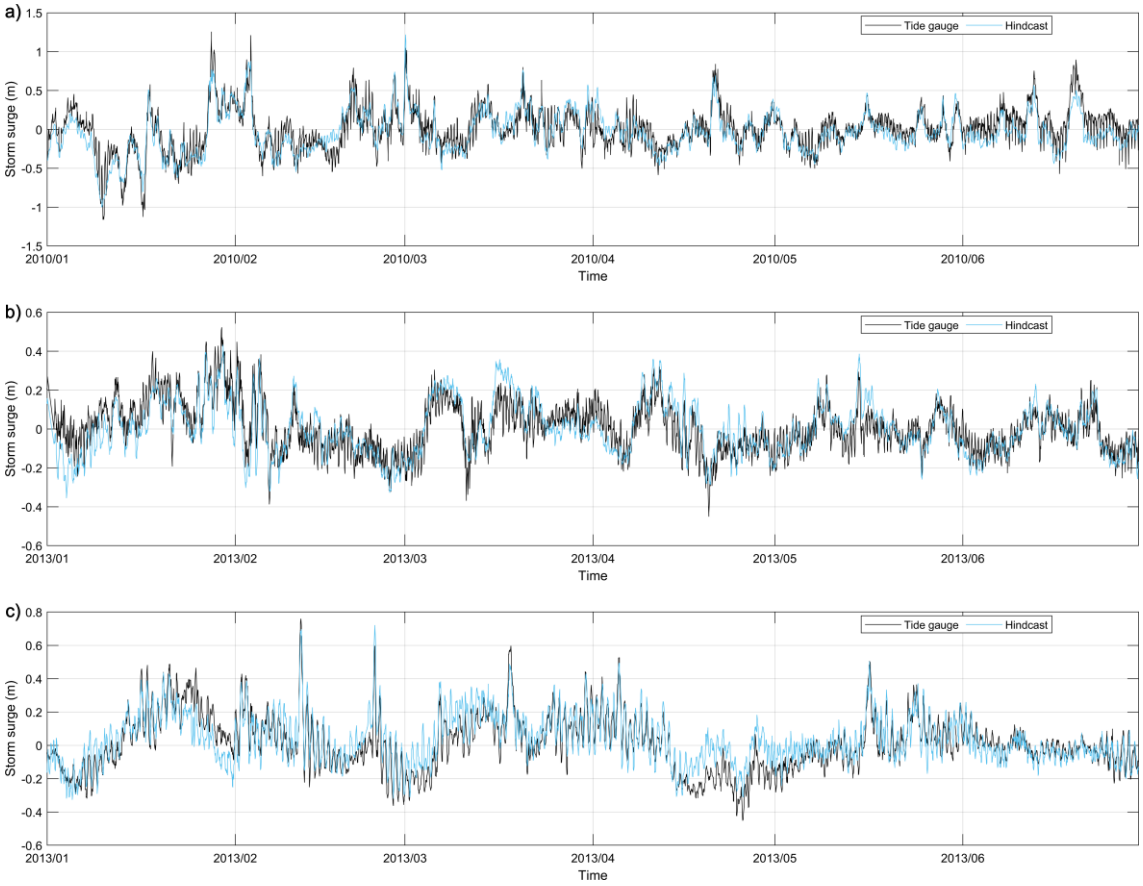

Figure S1: Hourly time series of storm surge from the storm surge hindcast and non-tidal residual sea level from tide-gauge observations. (a) Cuxhaven (Germany, North Sea), (b) Cherboug (France, British channel), and (c) Venice (Italy, Mediterranean Sea).

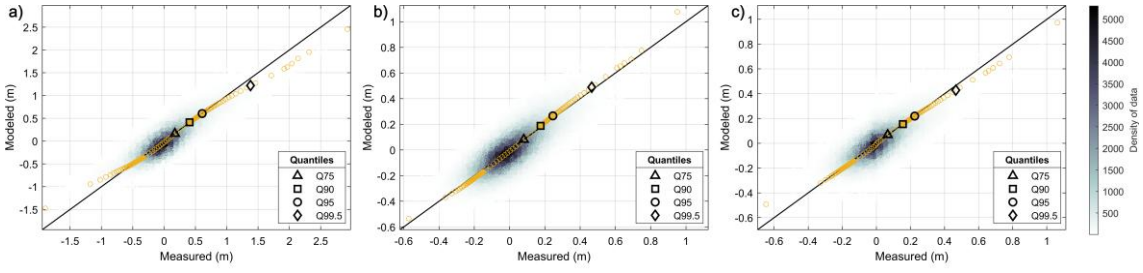

Figure S2: Scatter plot (gray colormap) and quantile–quantile plot (yellow circles and markers) comparing tide-gauge observations (measured) with the storm surge hindcast (modeled). (a) Cuxhaven (Germany, North Sea), (b) Cherboug (France, British channel), and (c) Venice (Italy, Mediterranean Sea).

As shown in the previous figures, the storm surge hindcast dataset exhibits excellent performance in reproducing the temporal evolution of storm surge events, particularly the peak values observed during storm events. An underestimation of maxima

above the 99.5th percentile and an overestimation of minima below the 10th percentile is observed at many tide-gauge stations. These differences between simulated and observed data may be attributed to local effects at the tide-gauge stations, which are often located in estuaries, harbors, or complex coastal areas where the tidal signal is distorted by nearshore processes that cannot be resolved by the spatial resolution of the ROMS grid cells. The underestimation of some storm surge maxima may also result from the ERA5 wind fields, as several studies (e.g., Chen et al., 2024) have reported a systematic underestimation of ERA5 wind speeds during extratropical cyclone events. Table S1 shows the RMSE and bias metrics between modeled and observed storm surge data. The RMSE at most stations is below 10 cm. Biases are consistently below 2 cm, with a systematic underestimation observed along the North Sea coasts.

Table S1: Information on the tide-gauge stations used for validation. Tide-gauge station names, coordinates, RMSE, and bias values from the validation of the storm surge hindcast at each location.

	Tide gauge	Location		RMSE (cm)	BIAS (cm)
		Latitude	Longitude		
1	Vigo	42.243	-8.726	7.447	0.023
2	A Coruña	43.364	-8.399	6.840	-0.073
3	Ferrol	43.463	-8.326	7.434	0.000
4	Gijón	43.558	-5.698	7.130	-0.054
5	Santander	43.461	-3.791	6.732	-0.053
6	Bilbao	43.357	-3.05	7.124	0.044
7	Barcelona	41.342	2.163	7.430	0.006
8	Catania	37.498	15.094	6.193	-0.149
9	Livorno	43.546	10.299	6.736	-0.351
10	Ancona	43.625	13.506	8.046	-0.639
11	Imperia	43.878	8.019	6.087	-0.241
12	Genova	44.41	8.925	6.105	-0.331
13	Ravenna	44.492	12.283	8.555	-0.652
14	Venezia	45.418	12.426	8.989	-0.691
15	Trieste	45.649	13.759	9.582	-0.523
16	Nice	43.695	7.285	6.024	-0.234
17	Monaco	43.733	7.424	5.939	-0.192
18	Port Bloc	45.568	-1.062	9.130	-0.630
19	La Rochelle	46.148	-1.226	9.707	-0.628
20	Brest	48.383	-4.495	8.209	-0.753
21	Cherbourg	49.651	-1.635	8.678	-0.703
22	Calais	50.969	1.868	13.121	-0.903
23	Dunkerque	51.048	2.367	13.277	-1.151
24	St Marys	49.918	-6.315	7.851	-0.594
25	Newlyn	50.103	-5.543	8.189	-0.613
26	Cromer	52.934	1.301	10.326	-1.292
27	Whitby	54.483	-0.616	8.982	-1.079
28	North Shields	55.007	-1.439	8.940	-1.074
29	Aberdeen	57.15	-2.083	8.657	-1.103
30	Stornoway	58.207	-6.389	9.307	-1.238
31	Wick	58.433	-3.083	9.002	-1.252
32	Lerwick	60.154	-1.138	8.383	-1.030
33	Castletownbere	51.649	-9.903	7.751	-0.564
34	Malinhead	55.367	-7.333	8.204	-1.219
35	Cuxhaven	53.868	8.717	16.696	-2.172
36	Helgoland	54.179	7.89	13.364	-2.319
37	Aarhus	56.15	10.217	9.878	-0.951
38	Goteborg	57.683	11.8	10.088	-1.190
39	Stockholm	59.325	18.082	10.385	-0.363
40	Tregde	58.006	7.566	8.812	-0.861
41	Helgeroa	58.995	9.856	9.464	-1.034
42	Viker	59.036	10.949	10.632	-0.988
43	Rorvik	64.867	11.25	9.463	-1.176
44	Kabelvaag	68.212	14.482	9.637	-1.261
45	Andenes	69.326	16.135	9.576	-0.969

46	Vardo	70.333	31.1	9.147	-0.820
47	Honningsvag	70.98	25.973	9.026	-0.940
48	Reykjavik	64.15	-21.933	7.730	-0.560

Wind-waves

The offshore wave dataset was obtained from a wave hindcast developed using the third-generation numerical wave model WaveWatchIII (WW3; Tolman, 2009), version 7.00. The wave spectral domain is discretized into 24 directions and 32 non-linearly spaced frequencies ranging from 0.0373 Hz to 0.7159 Hz, with a frequency increment factor of 1.1. Bathymetry, land-sea masks, and obstruction grids were generated using the WW3 grid generation software (Chawla & Tolman, 2008). The model uses spatial fields of surface wind and sea ice concentration from the ERA5 reanalysis as input. A total of four domains were considered to design the multi-grid configuration of the regional wave hindcast. This configuration included a global regular grid with a spatial resolution of 1/2°, and two irregular (curvilinear) polar stereographic grids with a spatial resolution of 18 km in both directions, following an Irregular–Regular–Irregular (IRI) grid scheme (Rogers & Linzell, 2018). In addition, a regular grid covering the European Atlantic shelf and seas at 1/8° resolution was included. The physical formulation ST4 of Ardhuin et al. (2010) was adopted for wind input and energy dissipation, using the T471 parameterization (WW3DG, 2019). Default parameter values were used, except for the non-dimensional wind-wave growth parameter (β_{max}), which was tuned to calibrate the model for the ERA5 wind fields. The methodology proposed by Stopa (2018), based on satellite altimetry observations was adopted. The calibrated β_{max} parameter value of 1.46 was used for the simulations.

The DOW method (Camus et al., 2013) was setup and applied to obtain the nearshore wave database along the European coast. The nearshore wave hindcast was developed in four main steps: (i) sixteen unstructured numerical domains were designed to provide wave information at a coastal spatial resolution of l km, (ii) a total of 1,000 hourly sea-state cases, representative of both mean and extreme conditions, were selected from the offshore wave hindcast for each numerical domain, (iii) the 1,000 wave conditions were simulated using the SWAN (Simulating Waves Nearshore) model (Booij et al., 1999), (iv) continuous hourly time series of sea-state parameters at the coastal target points (CTPs) were reconstructed.

The selection of the 1,000 sea states to be propagated nearshore was based on significant wave height, mean period, and mean wave direction from the offshore wave hindcast for the European region, as well as on ERA5 wind fields and sea-ice coverage. The maximum-dissimilarity algorithm was applied over the principal components of these standardized variables to select the simulation cases. SWAN version 41.45 was used to perform the nearshore wave simulations. This version was selected for its improved physical formulations, particularly its ability to activate wave dissipation due to sea ice. Prior to the numerical simulation of the selected cases, the sensitivity of coastal wave conditions to sea level variations was assessed. Based on the results, each selected sea state was propagated at three different water levels in domains with meso- and macro-tidal ranges, resulting in 3,000 simulations per domain.

Finally, a comprehensive validation process was conducted for both the offshore and nearshore components of the wave hindcast. Validation was based on comparisons between the offshore and nearshore hindcast products and buoy observations. Wave buoy records were obtained from the quality-controlled Global Ocean Delayed Mode Wave Product dataset, provided by the Copernicus Marine Environment Monitoring Service (CMEMS). A total of 84 offshore buoys (i.e., farther than 5 km from the coastline) and 109 coastal buoys were selected along the European coast to validate the offshore and nearshore wave databases, respectively. Most of the analyzed buoys cover periods longer than 10-15 years.

For the offshore wave validation, comparison of significant wave height from the hindcast against 84 offshore buoys resulted in an average bias of –0.07 m and an RMSE of 0.34 m. Bias and RMSE values resulting for the nearshore hindcast compared with coastal buoy observations are shown in Figure S3. The spatial distribution of the bias shows both positive and negative values, which in most locations do not exceed an absolute value of 0.15 m. Positive biases are predominant in the Baltic Sea,

while negative biases prevail in the Mediterranean Sea and the Canary Islands. Other regions present a mix of positive and negative values, with several coastal aeras showing biases close to zero. RMSE values between 0.2 and 0.3 m are observed in the North Sea, the Baltic Sea, and most locations in the Mediterranean. Higher values are found in the Aegean Sea, Cantabrian Sea, English Channel, and around the British Isles.

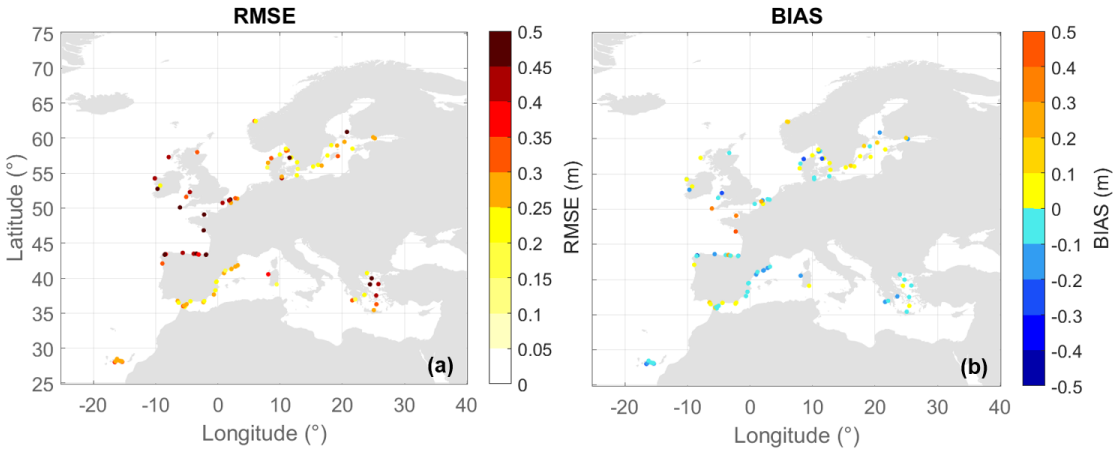

Figure S3: Spatial distribution of bias (left) and RMSE (right) in significant wave height (Hs, m) from the nearshore wave hindcast, evaluated at the locations of coastal wave buoys.

Supplementary figures and table

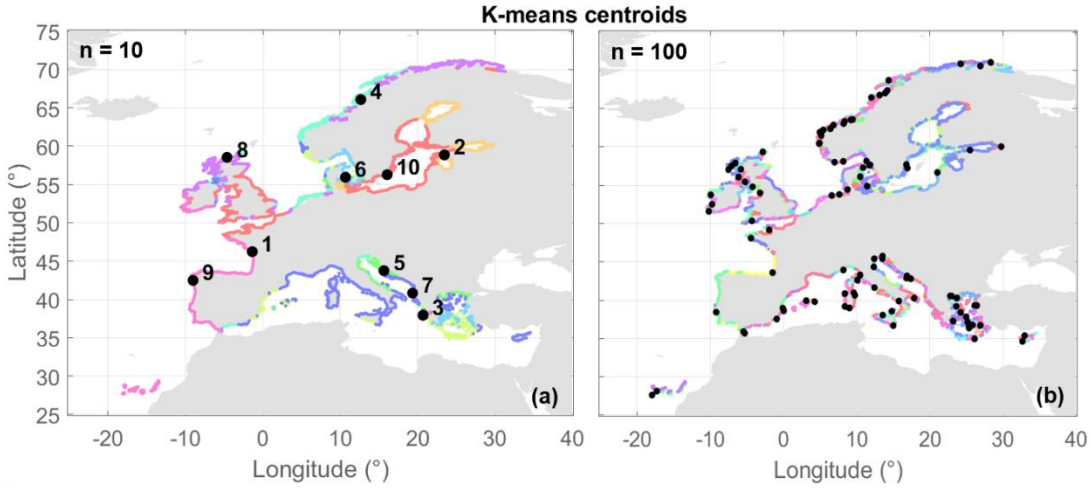

Figure S4: Selection of representative CTP to be used in the EVA preliminary tests and as examples throughout this study. Selection of 10 clusters with their respective centroids highlighted in black dots (a). Selection of 100 clusters with their respective centroids highlighted in black dots (b). Results were generated from a k-means clustering based on relative contributions of TWL components under mean conditions.

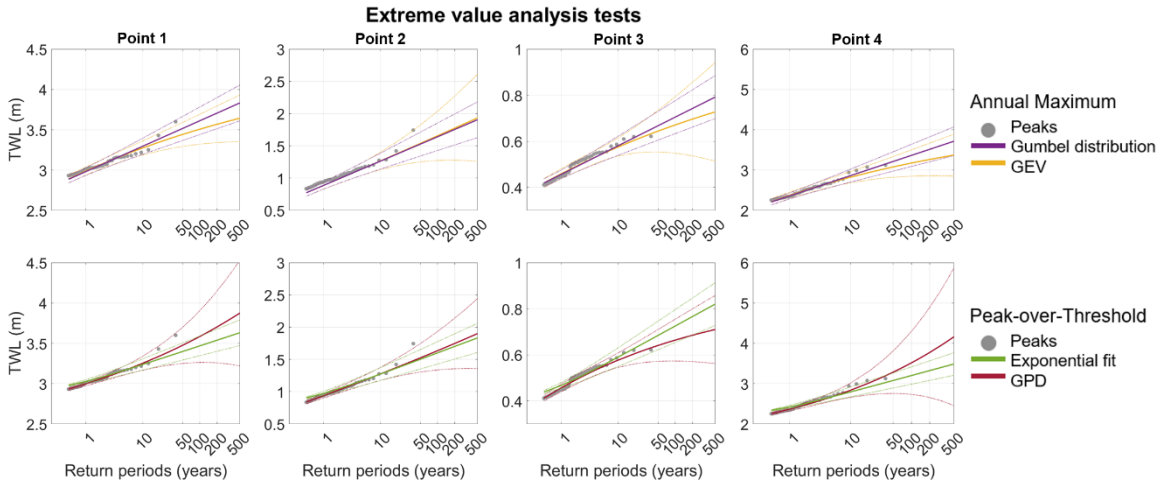

Figure S5: EVA tests performed for the first 10 centroids and shown for test points 1, 2, 3, and 4. Upper row shows results using annual maxima to select extreme events and distributions Gumbel and GEV to estimate return level events. Bottom row, peak-over-threshold with a threshold corresponding to a λ = 2, used in the present study, and distributions exponential and GPD to estimate return levels.

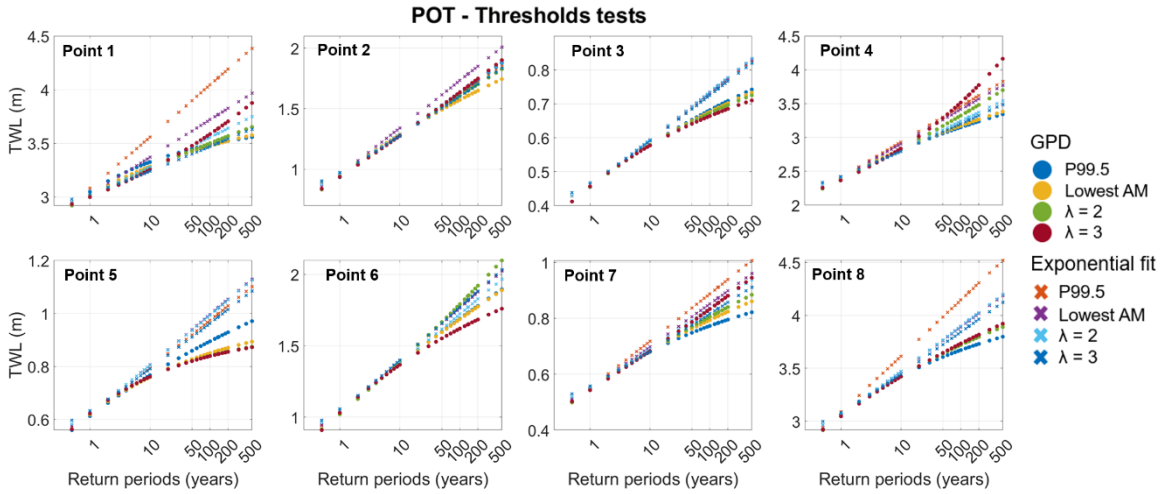

Figure S6: Threshold tests applied for peak-over-threshold method when selecting the historic sample of extremes events. Results are shown for both GPD and exponential fits for test points, 1, 2, 3, 4, 5, 6, 7, and 8.

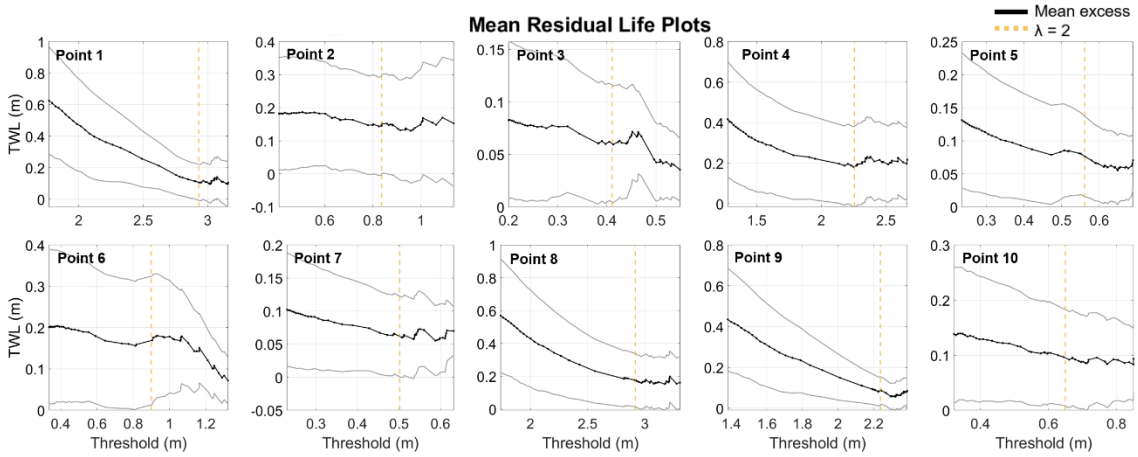

Figure S7: Mean residual life plots used to support the definition of a threshold for the POT method. Results are shown for the first 10 centroids used. Following Coles (2001), a stability in the plot indicates a potential value for a threshold. Yellow dashed lines indicate the TWL value correspondent to a λ = 2, used in the present study.

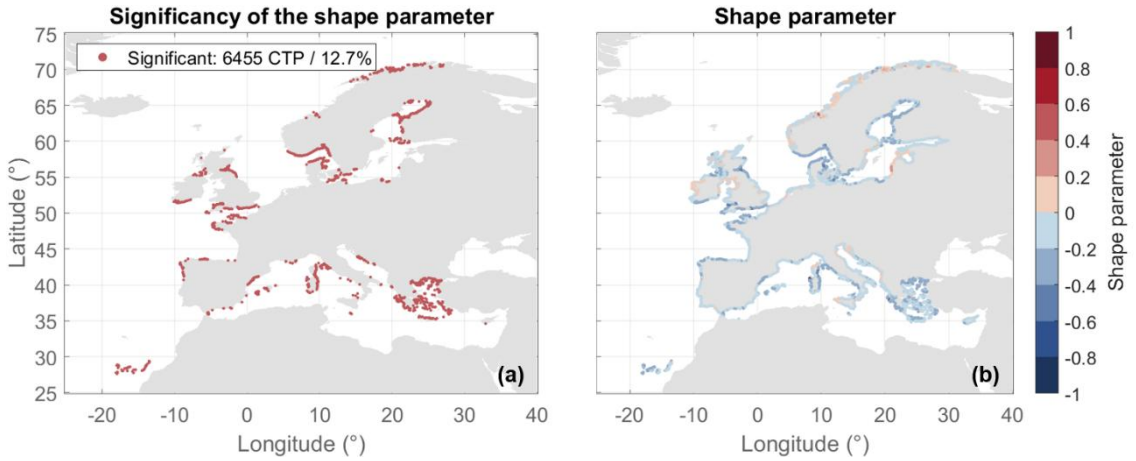

Figure S8: Spatial distribution of the Generalized Pareto Distribution (GPD) shape parameter (a) and their respective significancy to a 95th confidence level (b).

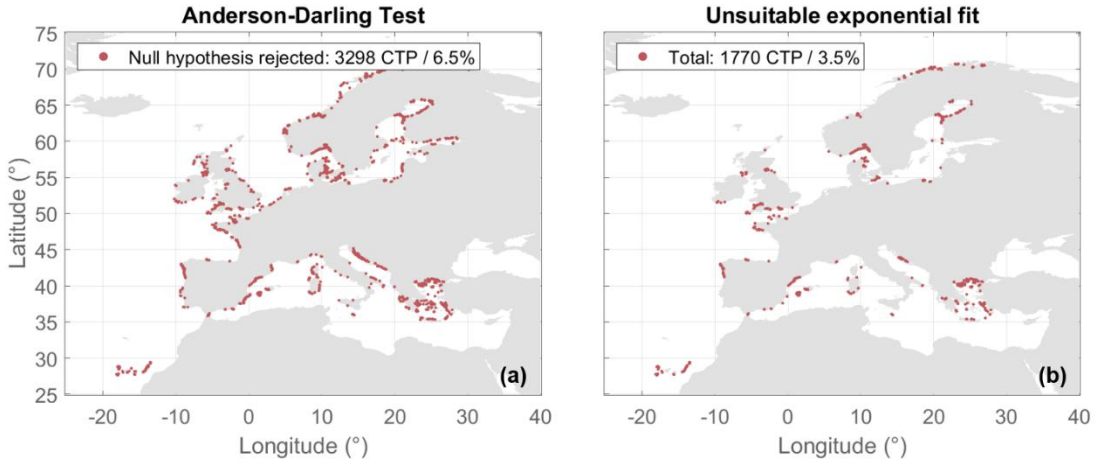

Figure S9 :Location of CTPs where the Anderson-Darling test resulted in a rejected null hypothesis (a). Location of CTPs where the GPD shape parameter was significant and the Anderson-Darling test null hypothesis was rejected (b), indicating where the exponential fit was unsuitable to estimate return levels.

Table S2: References used in the TWL reconstruction validation and the respective locations analyzed.

References	Locations validated
Breilh et al. (2013)	Brouage (FR)
Cabrita et al. (2024)	Porto Garibaldi (IT)
IHCantabria (2021a)	Santander (ES)
IHCantabria (2021b)	Murcia (ES)
Irazoqui Apecechea et al. (2023)	Hoek van Holland (NL), Huelva (ES), Kiel (DE), Marina Di Campo and Venice (IT), Valencia (ES)
Kiesel et al. (2023)	Koserow, Sassnitz , Schlei Fjord, and Wismar (DE), Klagshamn (SE)
Koks et al. (2023)	Ebel Estuary (DE), Rimini (IT)
Lemos et al. (2025)	Faro (PT)
Perini et al. (2015)	Porto Corsini (IT)
Scicchitano et al. (2021)	Catania, Portopalo di Camo Passero, and Sicily (IT), Malta (MT)
Wadey et al. (2012)	Lymington, Solent (UK)
Wolski & Wiśniewski (2021)	Wismar (DE), Korsor (DK), Parnu and Ristna (EE), Hamina and Kemi (FI), Swinoujscie (PL), Kungsholmsfort (SE)

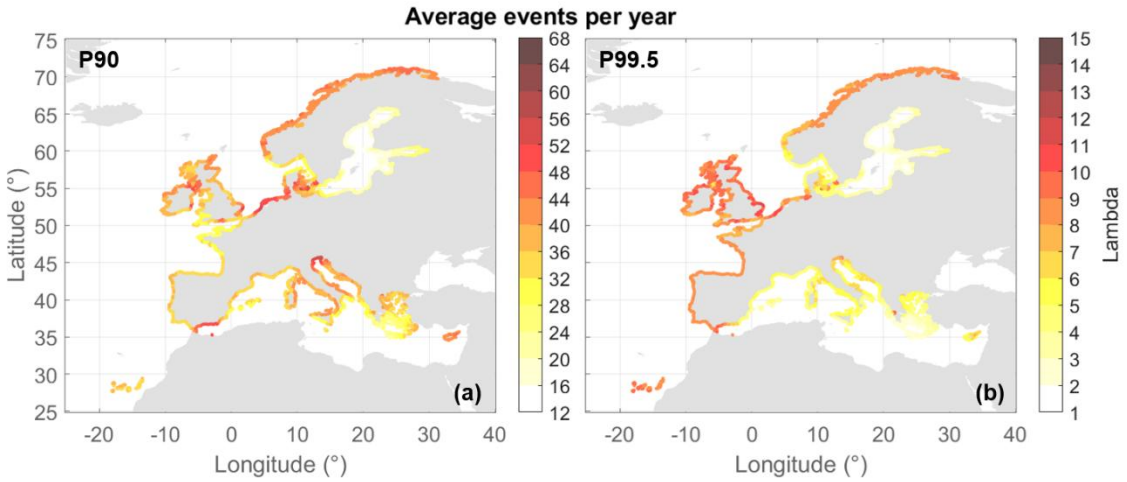

Figure S10: Spatial distributions of the λ (average events per year) resultant from a peak-over-threshold with a constant threshold of percentiles P90 (a) and P99.5 (b).

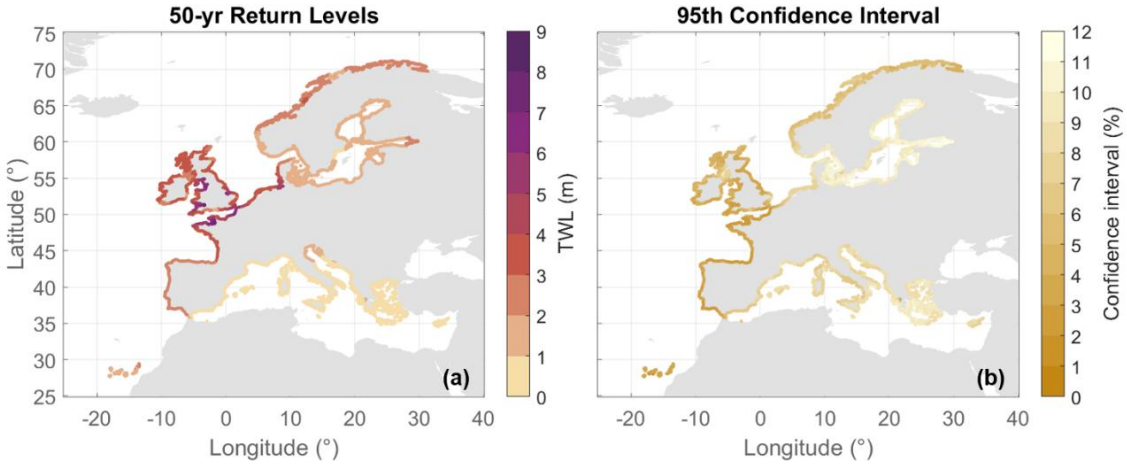

Figure S11: Spatial distribution of the 50-yr return period TWL resulting from POT with an exponential fit (a) and spatial distribution of the 50-yr confidence interval relative to the 50-yr TWL event, in percentage (b).

References

WW3DG, The WAVEWATCH III® Development Group. (2019). *User Manual and System Documentation of WAVEWATCH III® Version 6.07. Tech. Note 333, NOAA/NWS/NCEP/MMAB, College Park, MD, USA, 465 pp. Appendices*.

Ardhuin, F., Rogers, E., Babanin, A. V., Filipot, J. F., Magne, R., Roland, A., van der Westhuysen, A., Queffeulou, P., Lefevre, J. M., Aouf, L., & Collard, F. (2010). Semiempirical dissipation source functions for ocean waves. Part I: Definition, calibration, and validation. *Journal of Physical Oceanography*, *40*(9), 1917–1941. https://doi.org/10.1175/2010JPO4324.1

Booij, N., Ris, R. C., & Holthuijsen, L. H. (1999). A third-generation wave model for coastal regions 1. Model description and validation. *Journal of Geophysical Research: Oceans*, *104*(C4), 7649–7666. https://doi.org/10.1029/98JC02622

Breilh, J. F., Chaumillon, E., Bertin, X., & Gravelle, M. (2013). Assessment of static flood modeling techniques: Application to contrasting marshes flooded during Xynthia (western France). *Natural Hazards and Earth System Sciences*, *13*(6), 1595–1612. https://doi.org/10.5194/nhess-13-1595-2013

Cabrita, P., Montes, J., Duo, E., Brunetta, R., & Ciavola, P. (2024). The Role of Different Total Water Level Definitions in Coastal Flood Modelling on a Low-Elevation Dune System. *Journal of Marine Science and Engineering*, *12*(6), 1003. https://doi.org/10.3390/jmse12061003

Camus, P., Mendez, F. J., Medina, R., Tomas, A., & Izaguirre, C. (2013). High resolution downscaled ocean waves (DOW) reanalysis in coastal areas. *Coastal Engineering*, *72*, 56–68. https://doi.org/10.1016/j.coastaleng.2012.09.002

Chapman, D. C. (1985). Numerical treatment of cross-shelf open boundaries in a barotropic coastal ocean model. *Journal of*

Physical Oceanography, *15*(8), 1060–1075.

Chawla, A., & Tolman, H. L. (2008). Obstruction grids for spectral wave models. *Ocean Modelling*, *22*(1–2), 12–25. https://doi.org/10.1016/j.ocemod.2008.01.003

Cid, A., Castanedo, S., Abascal, A. J., Menéndez, M., & Medina, R. (2014). A high resolution hindcast of the meteorological sea level component for Southern Europe: the GOS dataset. *Climate Dynamics*, *43*(7–8), 2167–2184. https://doi.org/10.1007/s00382-013-2041-0

Codiga, D. L. (2011). *Unified Tidal Analysis and Prediction Using the UTide Matlab Functions*. *September*, 59. https://doi.org/10.13140/RG.2.1.3761.2008

Egbert, G. D., Bennett, A. F., & Foreman, M. G. G. (1994). TOPEX/POSEIDON tides estimated using a global inverse model. *Journal of Geophysical Research*, *99*(C12). https://doi.org/10.1029/94jc01894

Egbert, G. D., & Erofeeva, S. Y. (2002). Efficient inverse modeling of barotropic ocean tides. *Journal of Atmospheric and Oceanic Technology*, *19*(2), 183–204. https://doi.org/10.1175/1520-0426(2002)019<0183:EIMOBO>2.0.CO;2

Flather, R. A. (1976). A tidal model of the northwest European continental shelf. *Mem. Soc. Roy. Sci. Liege*, *10*, 141–164.

Haigh, I. D., Marcos, M., Talke, S. A., Woodworth, P. L., Hunter, J. R., Hague, B. S., Arns, A., Bradshaw, E., & Thompson, P. (2022). GESLA Version 3: A major update to the global higher-frequency sea-level dataset. *Geoscience Data Journal*, *10*(3), 293–314. https://doi.org/10.1002/gdj3.174

Hersbach, H., Bell, B., Berrisford, P., Hirahara, S., Horányi, A., Muñoz-Sabater, J., Nicolas, J., Peubey, C., Radu, R., Schepers, D., Simmons, A., Soci, C., Abdalla, S., Abellan, X., Balsamo, G., Bechtold, P., Biavati, G., Bidlot, J., Bonavita, M., De Chiara, G., Dahlgren, P., Dee, D., Diamantakis, M., Dragani, R., Flemming, J., Forbes, R., Fuentes, M., Geer, A., Haimberger, L., Healy, S., Hogan, R.J., Hólm, E., Janisková, M., Keeley, S., Laloyaux, P., Lopez, P., Lupu, C., Radnoti, G., de Rosnay, P., Rozum, I., Vamborg, F., Villaume, S., Thépaut, J. N. (2020). The ERA5 global reanalysis. *Quarterly Journal of the Royal Meteorological Society*, *146*(730), 1999–2049. https://doi.org/10.1002/qj.3803

IHCantabria, Instituto de Hidráulica de Cantabria (2021a). *Análisis de los riesgos del cambio climático en la costa de Cantabria: propuesta para la adaptación*.

IHCantabria, Instituto de Hidráulica de Cantabria (2021b). *Elaboración de la evaluación de impactos y riesgos de inundación y erosión debidos al cambio climático en la costa murciana*.

Irazoqui Apecechea, M., Melet, A., & Armaroli, C. (2023). Towards a pan-European coastal flood awareness system: Skill of extreme sea-level forecasts from the Copernicus Marine Service. *Frontiers in Marine Science. 9:1091844* (Vol. 9). doi: 10.3389/fmars.2022.1091844

Kiesel, J., Lorenz, M., König, M., Gräwe, U., & Vafeidis, A. T. (2023). Regional assessment of extreme sea levels and associated coastal flooding along the German Baltic Sea coast. *Natural Hazards and Earth System Sciences*, *23*(9), 2961–2985. https://doi.org/10.5194/nhess-23-2961-2023

Koks, E. E., Le Bars, D., Essenfelder, A. H., Nirandjan, S., & Sayers, P. (2023). The impacts of coastal flooding and sea level rise on critical infrastructure: a novel storyline approach. *Sustainable and Resilient Infrastructure*, *8*(sup1), 237–261. https://doi.org/10.1080/23789689.2022.2142741

Lemos, G., Soares, P. M. M., Simões, R., Antunes, C., Bosnic, I., & Pinto, C. (2025). A physical climate storyline for the Hercules storm in Portugal: Extreme coastal flooding in southwestern Europe under a changing climate. *Science of the Total Environment*, *971*(March). https://doi.org/10.1016/j.scitotenv.2025.179050

Perini, L., Calabrese, L., Lorito, S., & Luciani, P. (2015). Il rischio da mareggiata in Emilia-Romagna: l'evento del 5-6 Febbraio 2015. *Il Geologo Volume*, *53*(January), 8–17.

Rogers, W. E. R., & Linzell, R. S. (2018). *The IRI Grid System for Use with WAVEWATCH III®, NRL Memorandum Report*. 47.

Scicchitano, G., Scardino, G., Monaco, C., Piscitelli, A., Milella, M., De Giosa, F., & Mastronuzzi, G. (2021). Comparing impact effects of common storms and Medicanes along the coast of south-eastern Sicily. *Marine Geology*, *439*(March), 106556. https://doi.org/10.1016/j.margeo.2021.106556

Shchepetkin, A. F., & McWilliams, J. C. (2005). The regional oceanic modeling system (ROMS): A split-explicit, free-surface, topography-following-coordinate oceanic model. *Ocean Modelling*, *9*(4), 347–404. https://doi.org/10.1016/j.ocemod.2004.08.002

Stopa, J. E. (2018). Wind forcing calibration and wave hindcast comparison using multiple reanalysis and merged satellite wind datasets. *Ocean Modelling*, *127*(March), 55–69. https://doi.org/10.1016/j.ocemod.2018.04.008

Tolman, H. L. (2009). User manual and system documentation of WAVEWATCH-IIITM version 3.14. *Technical Note*, *3.14*, 220.

Wadey, M. P., Nicholls, R. J., & Hutton, C. (2012). Coastal flooding in the solent: An integrated analysis of defences and

inundation. *Water (Switzerland)*, *4*(2), 430–459. https://doi.org/10.3390/w4020430

Wolski, T., & Wiśniewski, B. (2021). Characteristics and long-term variability of occurrences of storm surges in the baltic sea. *Atmosphere*, *12*(12). https://doi.org/10.3390/atmos12121679